Journal of Materials Chemistry A

ROYAL SOCIETY OF CHEMISTRY

PAPER

View Article Online
View Journal | View Issue

Check for updates

Cite this: J. Mater. Chem. A, 2021, 9, 18498

Microstructural origin of selective water oxidation to hydrogen peroxide at low overpotentials: a study on Mn-alloyed TiO_2†

Jiahui Li,‡[abc] Devan Solanki,‡[ab] Qianhong Zhu,[a] Xin Shen,[ab] Grace Callander,[ab] Jaehong Kim,[a] Yaogang Li,[c] Hongzhi Wang *[c] and Shu Hu *[ab]

One key objective in electrocatalysis is to design selective catalysts, particularly in cases where the desired products require thermodynamically unfavorable pathways. Electrochemical synthesis of hydrogen peroxide (H_2O_2) *via* the two-electron water oxidation reaction ($2e^-$ WOR) requires a +0.54 V higher potential than four-electron O_2 evolution. So far, best-performing electrocatalysts require considerable overpotentials before reaching peak faradaic efficiency. We present Mn-alloyed TiO_2 coatings prepared by atomic layer deposition (ALD) and annealing as a stable and selective electrocatalyst for $2e^-$ WOR. Faradaic efficiency of >90% at < 150 mV overpotentials was achieved for H_2O_2 production, accumulating 2.97 mM H_2O_2 after 8 hours. Nanoscale mixing of Mn_2O_3 and TiO_2 resulted in a partially filled, highly conductive Mn^{3+} intermediate band (IB) within the TiO_2 mid-gap to transport charge across the (Ti,Mn) O_x coating. This IB energetically matched that of H_2O_2-producing surface intermediates, turning a wide bandgap oxide into a selective electrocatalyst capable of operating in the dark. However, the high selectivity is limited to the low overpotential regime, which limits the system to low current densities and requires further research into increasing turn-over frequency per active site.

Received 28th June 2021
Accepted 4th August 2021

DOI: 10.1039/d1ta05451a

rsc.li/materials-a

Published on 05 agosto 2021. Downloaded on 06/05/2026 15:02:15.

1. Introduction

Hydrogen peroxide (H_2O_2) is an important green oxidant[1] routinely used for chemical and environmental applications[2] such as pulp bleaching,[3] chemical-mechanical actuation,[4] water treatment, and disinfection.[5] In addition, H_2O_2 is receiving growing interest as a potential energy carrier, capable of long-duration energy storage.[6] H_2O_2 is primarily produced by the anthraquinone oxidation process.[2,7] However, this process involves sequential hydrogenation and oxidation steps which require energy-intensive gas transport and product separation—processes only economical at plant-scale, hindering distributed use for water treatment or disinfection. Direct synthesis of H_2O_2 from H_2 and O_2 over heterogeneous catalysts is one route for distributed synthesis,[8] but recently, (photo-) electrochemical synthesis of H_2O_2 which uses abundant water or air as feedstock and renewable electricity or sunlight as energy inputs has provided an attractive alternative to the industrial anthraquinone-based process.[9]

H_2O_2 can be (photo-)electrochemically synthesized *via* a two-electron ($2e^-$) water oxidation pathway, as shown in eqn (1):

$$2H_2O \rightarrow H_2O_2 + 2H^+ + 2e^-,\ E = +1.77\ V_{RHE} \quad (1)$$

However, existing catalysts often exhibit low faradaic efficiency (FE) due to the competitive four-electron ($4e^-$) pathway of O_2 evolution reaction (OER; eqn (2)):

$$2H_2O \rightarrow O_2 + 4H^+ + 4e^-,\ E = +1.23\ V_{RHE} \quad (2)$$

The thermodynamic driving force for OER is always at least +0.54 V greater than that of the $2e^-$ H_2O_2 pathway which can allow the undesired O_2 evolution pathway to overcome any kinetic barriers and dominate. In addition, the produced H_2O_2 can be over-oxidized to O_2 at an excess potential of at least +1.09 V (eqn (3)):

$$H_2O_2 \rightarrow O_2 + 2H^+ + 2e^-,\ E = +0.68\ V_{RHE} \quad (3)$$

Finally, catalytic surfaces should not disproportionate the adsorbed H_2O_2 molecules:

$$2H_2O_2 \rightarrow 2H_2O + O_2 \quad (4)$$

[a]Department of Chemical and Environmental Engineering, Yale University, New Haven, Connecticut 06520, USA. E-mail: shu.hu@yale.edu

[b]Energy Sciences Institute, Yale University, 810 West Campus Drive, West Haven, Connecticut 06516, USA

[c]State Key Laboratory for Modification of Chemical Fibers and Polymer Materials, College of Materials Science and Engineering, Donghua University, Shanghai 201620, People's Republic of China. E-mail: wanghz@dhu.edu.cn

† Electronic supplementary information (ESI) available. See DOI: 10.1039/d1ta05451a

‡ Jiahui Li and Devan Solanki contributed equally.

This journal is © The Royal Society of Chemistry 2021

Published on 05 agosto 2021. Downloaded on 06/05/2026 15:02:15.

Thus, the selectivity of $2e^-$ water oxidation reaction (WOR) represents a common conundrum in electrocatalysis and strategies to address this challenge can be broadly applicable.[9–11]

Various water-oxidation materials have been both experimentally and theoretically investigated, including aluminum porphyrins,[12] carbon-based materials,[13] $BiVO_4$,[14,15] WO_3,[16] $CaSnO_3$,[17] and various composite materials.[18] Several electrocatalytic[19] and photoelectrocatalytic[15] systems have showed faradaic efficiency (FE) values as high as 86%. However, best performing $2e^-$ WOR catalysts ZnO[20] and $CaSnO_3$ (ref. 17) reach their peak FE at +2.6 V_{RHE} and +3.2 V_{RHE}, respectively, requiring considerable overpotentials to reach the 81% and 76% FE for H_2O_2 selectivity, respectively. Thus, strategies to achieve high selectivity at low overpotentials should be a major milestone for the field.

MnO_x is a conductive oxide that has been used for H_2O_2 production.[21] However, MnO_x has not been successfully utilized in aqueous environments as it is capable of $4e^-$ O_2-evolution and has been shown to disproportionate H_2O_2. TiO_2-rich surfaces may be promising for H_2O_2 production, since TiO_2 is ineffective for either O_2 evolution or H_2O_2 decomposition. Typically, TiO_2 undergoes a $1e^-$ pathway to produce $OH^\bullet$, which then produces H_2O_2 or O_2.[22]

In this study, the authors synthesize Mn-alloyed TiO_2 *via* atomic layer deposition (ALD), denoted as (Ti,Mn)O_x. The introduction of Mn 3d electronic states leads to the formation of a highly conductive Mn IB inside the otherwise forbidden bandgap of an oxide coating. Based on materials characterizations, we confirmed the nanoscale mixing of conductive and catalytically active phases otherwise not possible without ALD and post-growth annealing. We then investigated the effects of the electronic tuning of TiO_2 and found that the nanocrystalline microstructure resulted in a multifunctional electrocatalyst for selective water oxidation to hydrogen peroxide.

2. Experimental methods

2.1 Atomic layer deposition

The composite (Ti,Mn)O_x films were grown by using 2, 4, 8, or 16 ALD cycles of TiO_2 per 1 cycle of MnO_x, which are denoted as 2 : 1, 4 : 1, 8 : 1, and 16 : 1 (TiO_2 : MnO_x) films (ESI S1†). Tetrakis-dimethylamido-titanium (TDMAT, Sigma-Aldrich, 99.999%) and bis-(ethyl-cyclopentadienyl) manganese ($Mn(EtCp)_2$, Strem Chemicals, 99.999%) precursors for ALD were used as the Ti and Mn sources, respectively. The growth rates of MnO_x and TiO_2 were 0.97 and 0.47 Å per cycle, respectively. The MnO_x cycle was placed in the middle of the TiO_2 cycles. For example, 4 : 1 cycle ratio should lead to TiO_2-rich surfaces with subsurface Mn atoms. The sequences for each film composition were repeated until each film reached the desired thickness of *ca.* 50 nm. All (Ti,Mn)O_x films were annealed in air at 500 °C for 2 hours and oven cooled. For electrocatalysis, fluorine-doped tin oxide (FTO) substrates were used, while fused silica substrates were used for material characterizations. The Mn elemental composition was correlated with, but not equal to, the nominal cycle ratio.

2.2 Electrochemical measurements

The electrochemical behavior of (Ti,Mn)O_x electrodes was measured with a three-electrode setup. A Bio-Logic S200 potentiostat system connected the (Ti,Mn)O_x working electrode, saturated Ag/AgCl reference electrode, and Ti foil counter electrode. The Ti counter electrode was chosen to keep consistent with a previous study.[14] A cation exchange membrane separates the (TiMn)O_x and Ti foil electrodes to confine the H_2O_2 production in the working electrode compartment. Cyclic voltammetry was acquired with a scan rate of 20 mV s^{-1}.

2.3 H_2O_2 quantification

FE for H_2O_2 production was quantified by measuring the molar quantities of accumulated H_2O_2 produced by 4 : 1 (Ti,Mn)O_x as a function of current densities (geometric electrode area), ranging from 0.1 to 5.0 mA cm^{-2} (Fig. 2c). H_2O_2 concentration was quantified and validated using multiple titration methods in an H-type membrane cell (S1.5).† High-performance liquid chromatography (HPLC, Fig. S15†) quantification was used only to validate product identity and titration precision. Extended discussion can be found in ESI (S1.5 H_2O_2 quantification).†

2.4 XPS characterization of intermediate-band electronic structures

Valence band XPS was used to characterize the electronic structures of catalytic surfaces. The valence XPS spectra of the (Ti,Mn)O_x films were compared with that of a pure TiO_2 film and used to derive the IB energy levels in a band diagram.[23] Peak deconvolution was conducted under the following assumptions: (1) bandgap measurements for MnO_x-alloyed TiO_2 by UV-Vis spectroscopy (Fig. S9†) showed that (Ti,Mn)O_x bandgaps remain the same as pure TiO_2 (2) extended X-ray absorption fine structure (EXAFS) characterizations (Fig. S10†) show the presence of Mn–Mn feature as the second coordination shell, indicating that MnO_x forms clusters or nanocrystals inside the host oxide of crystallized TiO_2. Therefore, we consider the 4 : 1 (Ti,Mn)O_x, coating has nanoscale mixing of rutile TiO_2 and bixbyite Mn_2O_3 crystallites, and therefore contains two types of oxygen, one bridging neighboring Ti atoms and the other connecting neighboring Mn atoms. Each type has a set of non-overlapping O 2p–π and O 2p–σ peaks. Therefore, the peak deconvolution involved six peaks for 4 : 1(Ti,Mn)O_x.

Valence XPS analysis of pure TiO_2 resulted in two main peaks. This analysis is discussed later in the paper and presented in Fig. 4. One peak occurred at the binding energy (BE) of 7.10 eV and the other peak occurred at 5.03 eV.[24] The valence XPS spectra of 4 : 1 (Ti,Mn)O_x has two extra oxygen peaks that are slightly (~0.3 eV) more negative to these two peaks. In addition to the oxygen peaks, two additional peaks were assigned to the Mn 3d states. The Mn 3d-t_{2g} and Mn 3d-e_g bands corresponded to the Mn $3d_{3/2}$ and Mn $3d_{5/2}$ peaks, respectively.[25,26] The two primary O 2p peaks were still assigned at 7.10 ± 0.10 eV and 4.90 ± 0.10 eV, while the two Mn 3d peaks were located at 3.03 ± 0.10 eV and 1.14 ± 0.10 eV. All these peaks are

Published on 05 agosto 2021. Downloaded on 06/05/2026 15:02:15.

referring to Fermi level position (E_F, designated at zero binding energy using Au calibration standards, as shown in Fig. S11†).

3. Results & discussion

As deposited (Ti,Mn)O_x contains atomically mixed Mn and Ti atoms in an amorphous phase due to the 150 °C growth temperature.[27] After annealing, diffraction peaks of 4 : 1 (Ti,Mn)O_x (Fig. 1a) indicate mixed nanocrystalline phases of rutile TiO_2 (PDF#01-078-1510) and bixbyite Mn_2O_3 (PDF#00-041-1442). Bixbyite Mn_2O_3 represented the dominant phase for annealed 2 : 1 and 4 : 1 (Ti,Mn)O_x while rutile represented the dominant phase for annealed 8 : 1 and 16 : 1 (Ti,Mn)O_x as no obvious XRD peaks for Mn_2O_3 were observed. However, extended X-ray absorption fine structure analysis at the Ti and Mn edges of the annealed 4 : 1 (Ti,Mn)O_x (Fig. S10†) revealed distinct second coordination shells for both Ti and Mn elements, consistent with the nanocrystallinity of both TiO_2 and Mn_2O_3 in the annealed coating.

Thus, rutile TiO_2 is present in 4 : 1 (Ti,Mn)O_x, and XRD analysis represents only a starting point for understanding the microstructure of (Ti,Mn)O_x, which is the topic of a further report. Diffraction peaks of annealed ALD TiO_x without Mn alloying indicated anatase TiO_2. Therefore, Mn-alloyed TiO_x results in a tuned electronic structure due to a proportion of common anion mixed-metal bonds, which are distinctive from previously reported mixed Ti–Mn oxides.[28,29]

Plan-view (Fig. 1b) and cross-sectional SEM images of (Ti,Mn)O_x (Fig. S1†) indicate a conformal coating with a uniform thickness on the FTO substrate. TEM images (Fig. S4†) showed that Mn_2O_3 crystallites were uniformly distributed across the (Ti,Mn)O_x surface due to the diffusion of Mn atoms and Mn_2O_3 ripening during annealing. Image analysis indicated that the average sizes of Mn_2O_3 grains were 4.5 ± 0.5 and 7.7 ± 0.5 nm for 4 : 1 and 2 : 1 (Ti,Mn)O_x, respectively. The TEM images showed bending contours, suggesting residual strain in the annealed films. Williamson–Hall analysis of the GI-XRD data suggested a strained status of Mn_2O_3 crystallites with 0.5% lattice tension. The fitted crystallite sizes were consistent with the analysis of TEM bright-field images.

XPS core-level spectroscopy was used to quantify the surface composition of rutile TiO_2 and bixbyite Mn_2O_3 (see Fig. S2†) and to verify the Mn^{3+} oxidation state (see Table S2 and ESI Results S2.1†). Angle-resolved X-ray photoelectron spectroscopy (XPS) indicated uniform compositional distribution of Ti and Mn from the surface to the bulk (Fig. S3†). The 4 : 1 (Ti,Mn)O_x has 36.09 at% of Mn within the 3 nm skin depth of the coating surface.

(*J*–*E*) behavior of (Ti,Mn)O_x in a phosphate-buffered (PB) solution of pH 7 (Fig. 2a), revealed that current density correlated with increasing Mn concentration. The films, except for 16 : 1 which was resistive due to sparse Mn concentration, share a similar on-set potential of approximately +1.8 V_{RHE}. Annealed ALD MnO_x showed no activity for H_2O_2 production and annealed TiO_2 did not generate significant currents (Fig. S5†). Numerous O_2 bubbles were observed on the annealed Mn_2O_3 control and at the cell sidewall. The redox feature of annealed MnO_x cyclic voltammogram (Fig. S5b†) agrees with previous reports, which indicated the stable OER window at +1.6–1.8 V_{RHE} and the formation of Mn(VII) species when the potential is above of +1.8 V_{RHE}.[30] These findings indicate that catalytic activity is dependent on alloying TiO_2 with Mn_2O_3 nanocrystallites. Though 2 : 1 and 4 : 1 have similar *J*–*E* behavior, the crystal grain sizes for 2 : 1 (Ti,Mn)O_x of 7.7 ± 0.5 nm made it difficult to maintain a TiO_2-rich surface. As surface MnO_x compounds are known to disproportionate H_2O_2 in aqueous environments, 2 : 1 (Ti,Mn)O_x would pose challenges accumulating H_2O_2,[31] and thus 4 : 1 (Ti,Mn)O_x was chosen as the focus of this study.

J–*E* behavior measured in pH 3 and 9 PB solutions (Fig. S6†) showed similar trends, however, the pH 7 PB solution was chosen as the electrolyte for further testing to be compatible with reported membrane-free electrolyte-free H_2O_2 electrolysis designs that minimize transport loss.[32]

The onset potentials (at $J = 0.2$ mA cm^{-2}) of 4 : 1 (Ti,Mn)O_x (Fig. 2b) was +1.89 V_{RHE}, comparable to +1.90 and +1.96 V_{RHE} for

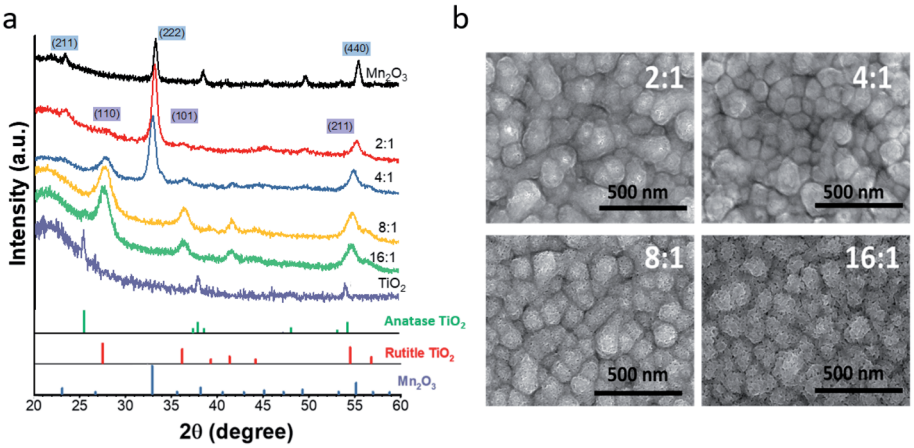

Fig. 1 (a) Grazing incident X-ray diffraction (GI-XRD) spectra and (b) plan-view scanning electron microscope (SEM) images of annealed (Ti,Mn)O_x. Samples denoted Mn_2O_3 and TiO_2 represent annealed ALD MnO_x and TiO_x, respectively.

 This journal is © The Royal Society of Chemistry 2021

Published on 05 agosto 2021. Downloaded on 06/05/2026 15:02:15.

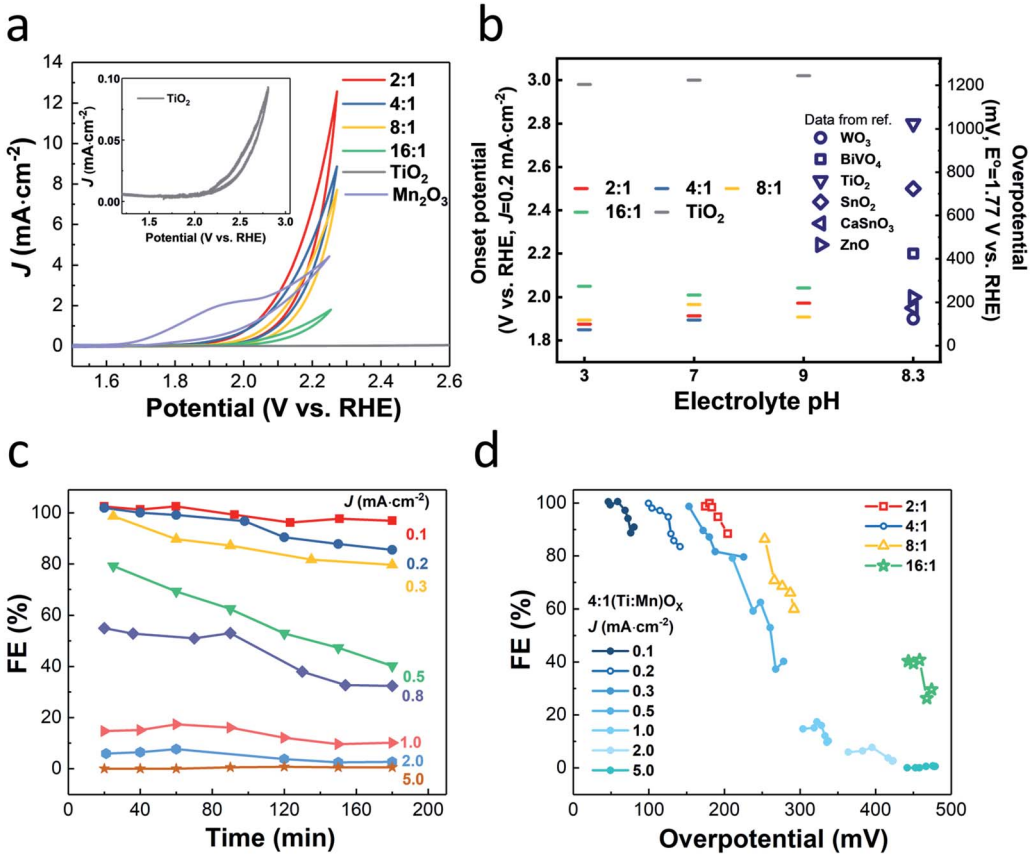

Fig. 2 Electrochemical performance. (a) J–E behavior of (Ti,Mn)O_x in 0.5 M pH = 7 phosphate buffer at a scan rate of 20 mV s^{-1}, (b) onset potentials at the respective J = 0.2 mA cm^{-2} (left y-axis) and overpotentials (right y-axis) derived from the (Ti,Mn)O_x J–E curves, plotted together with the data obtained from references of WO_3, $BiVO_4$, TiO_2, and SnO_2,[10] ZnO,[20] and $CaSnO_3$.[17] The measurement error for overpotentials is ± 0.02 V. (c) FE *vs.* electrolysis time using a 4 : 1 (Ti,Mn)O_x coating. (d) FE *vs.* overpotential at various current densities for the 4 : 1 (Ti,Mn)O_x coating in (c), overlaid with the FEs for 2 : 1, 8 : 1, and 16 : 1 (Ti,Mn)O_x films at J = 0.2 mA cm^{-2}.

the 2 : 1 and 8 : 1 films, respectively. The onset potentials of the (Ti,Mn)O_x coatings are non-variant in changing pH (Fig. 2b) and follow the trend that 4 : 1 (Ti,Mn)O_x has the lowest onset potential. Onset potentials were lower than the many catalysts, including $BiVO_4$ (+2.20 V_{RHE}), TiO_2 (+2.80 V_{RHE}), SnO_2 (+2.50 V_{RHE}), and were comparable to WO_3 (+1.90 V_{RHE}).[14] $CaSnO_3$ reaches 0.2 mA cm^{-2} with an overpotential of 230 mV but requires +3.20 V_{RHE} to reach peak Faraday efficiency of 76%.[17] However, WO_3 was reported to be unstable due to surface H_2O_2 absorption, which may lead to low efficiency in the long term.[16]

Computational work suggests that there are optimal potential windows for H_2O_2 production, due to the competition with one-electron and four-electron oxidation reactions.[14] For 4 : 1 (Ti,Mn)O_x, FE values of over 95% were obtained at overpotentials less than 150 mV, *i.e.*, at +1.9 V_{RHE}, or at equivalent current densities of 0.1 mA cm^{-2}. As FE begins near unity at just above +1.77 V_{RHE} and decreases with increasing current density (Fig. 2c) or with increasing overpotentials, (Ti,Mn)O_x suffers from a small optimal potential window (Fig. 2d). However, this range of FE values was 20% higher than the highest reported FE of 66% for the hydrophobic carbon dark anode measured in $NaHCO_3$(aq).[14] The average FE of 98% at 0.1 mA cm^{-2} was comparable to reported photochemical results, such as a FE of 98% for $BiVO_4$ photoanodes[14] and a FE of 80% for $BiVO_4$–Al_2O_3 photoanodes.[33] However, when the current density was increased to 1.0 mA cm^{-2}, corresponding to an overpotential of 250 mV, the FE dropped to less than 20%, and while this decline in FE is undesirable, it is consistent with other reports which show that selectivity can drop off with increased overpotentials.[14] (Ti,Mn)O_x is unique as the measured FEs start >90% at near zero overpotentials and drop off while FE in other systems such as $BiVO_4$ and ZnO ramp up, whereas the FEs in other systems such as $BiVO_4$ and ZnO initially ramp up, reaching comparable selectivity only at >400 mV overpotentials.[14,20]

Electrochemical impedance spectroscopy (EIS) was used to correlate electrical conductivity with composition-dependent J–E behavior (Fig. S7 & Table S3†). Analyses showed that the charge-transport resistance through the coatings were 48.6, 47.2, 50.1, 78.0 Ω for the 2 : 1, 4 : 1, 8 : 1, and 16 : 1 films, respectively. The impedance data also provided an estimated roughness factor of 10.7, which is calculated by dividing the geometric area of the electrode by the electrochemical surface area (see ESI Results S2.2).†

Published on 05 agosto 2021. Downloaded on 06/05/2026 15:02:15.

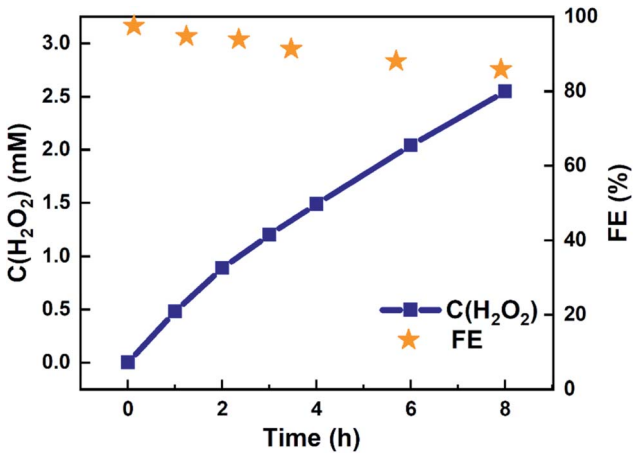

Fig. 3 H_2O_2 accumulation using 4 : 1 (Ti,Mn)O_x-coated FTO electrode operated in the dark. Cumulative H_2O_2 concentration and the respective cumulative FE *vs.* time. The electrode area was 1.2 cm^2, and the applied potential was +1.31 V *vs.* Ag/AgCl (equivalent to an overpotential of 150 mV) in a 20 mL 0.5 M pH = 7.0 PB solution.

Eight-hour electrolysis experiment using 4 : 1 (Ti,Mn)O_x in a batch reactor accumulated 2.97 mM of H_2O_2 in 20 mL, or 59.4 μmol (Table S4†). This accumulation was achieved in a static cell demonstrating that (Ti,Mn)O_x is capable of H_2O_2 desorption without overoxidation. As shown in Fig. 3, the cumulative FE begins near unity then gradually decreases to 85.8% after eight hours. However, this figure represents only the lower bound of FE as it does not account for product decomposition in the cell over the same period. As membranes have been reported to be highly effective at preventing H_2O_2 crossover between chambers, all of the H_2O_2 is accounted as being solely produced *via* WOR.[34,35]

We further tested the long-term stability for 4 : 1 (Ti,Mn)O_x in PB solutions of pH 5, 7, and 9 to evaluate its potential as a protective layer. Chronopotentiometry studies at 0.2 mA cm^{-2} showed a moderate increase in overpotential, with the electrode potentials increasing from +1.8 V_{RHE} to less than +2.1 V_{RHE} after 200 hours (Fig. S8†). The potential increase was partially accelerated by the formation of O_2 bubbles on the surface reducing the total surface area of the catalyst. As the chronopotentiometry experiment varies applied potential to sustain a current, this decrease in surface area led to an increase in required potentials during the constant current testing. As demonstrated in Fig. 2c, the selectivity towards H_2O_2 decreased at higher applied potentials, creating a feedback loop where higher applied potentials resulted in more oxygen generation. This process would slowly increase the required potential, until some breakdown voltage which would eventually lead to the failure of the coating. However, the coating was stable in all three pH conditions for over 200 hours, showing promise as protective coatings for semiconductors in corrosive environments.

The free energies of the relevant intermediates of the one, two, and four electron water oxidation reactions, *i.e.*, OH* and O* free energy have been shown to be key in determining reaction pathways.[14] While experimental evidence for the exact identity of the active site would allow for optimization and improved simulation, as recent literature has highlighted,[36,37] it can be challenging identifying the nanocrystalline active sites, even with advanced microscopy and EXAFS analysis. TiO_2 and MnO_x are on opposite sides of this volcano plot of a OH*-overpotential scaling relationship, with TiO_2 too large a OH* free energy and MnO_x not large enough.[38,39] Neither TiO_2 nor Mn_2O_3 is active for hydrogen peroxide production (Fig. S5a and b†), demonstrating that Mn-alloying is the necessary for activity. TiO_2 was chosen to be the surface termination layer as it was found not to disproportionate H_2O_2. Thus, (Ti,Mn)O_x promises favorable thermodynamics for selective peroxide production.

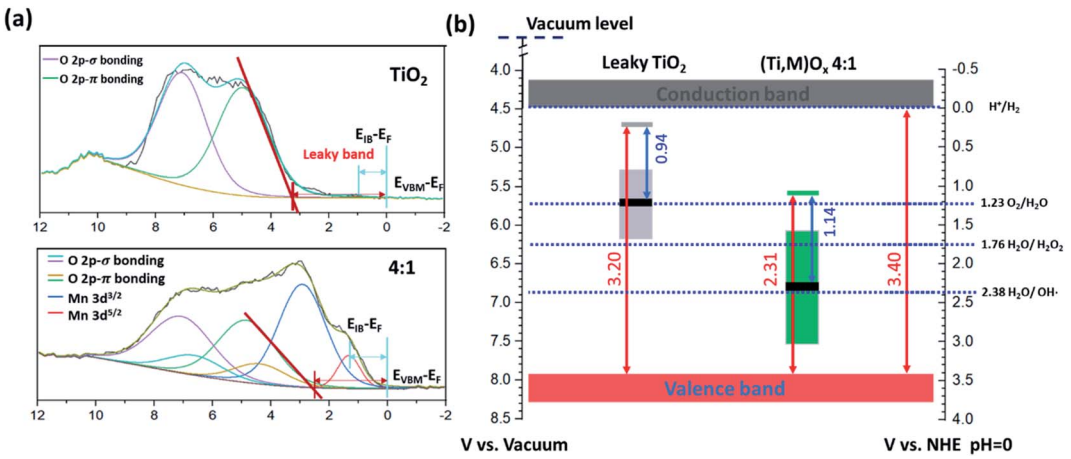

Fig. 4 Electronic structure characterizations of (Ti,Mn)O_x catalytic coatings. (a) Valence XPS spectra and (b) respective band diagrams (in the potential scale *versus* Reversible Hydrogen Electrode, RHE) of 4 : 1 (Ti,Mn)O_x and "leaky" TiO_2 surfaces. The positions of valence band maximum (E_{VBM}), intermediate band center (E_{IB}), and the Fermi level (E_F) are indicated in (a), and their respective energetics are drawn in (b). $E_{VBM} - E_F$ and $E_{IB} - E_F$ are labelled and are listed in Table S1.† The height of colored boxes indicates the full width at half maximum (FWHM) of Ti^{3+}-defect band (0.88 ± 0.10 eV) of "leaky" TiO_2 quoted from ref. 36, and of the Mn intermediate bands (Mn $3d_{5/2}$) derived from the valence spectra shown in (a). The energetic error from XPS analyses is ±0.10 eV.

 This journal is © The Royal Society of Chemistry 2021

Published on 05 agosto 2021. Downloaded on 06/05/2026 15:02:15.

Valence XPS analyses indicated that a spatially continuous Mn-impurity IB was located within the TiO_2 bandgap due to unfilled Mn 3d electronic states (see ESI Results S2.3†). The red arrows in Fig. 4b represent the relative difference in binding energy (BE) between the valence band maximum (VBM) and the Fermi level, namely $E_{VBM} - E_F$, while the blue arrows represent the difference of BE between the IB center and the Fermi level, $E_{IB} - E_F$. With the addition of Mn, the position of the E_F shifted towards the VBM. For instance, $E_{VBM} - E_F$ reduced from 3.20 V for pure TiO_2 (*i.e.*, E_F at 0.14 V_{RHE}) to 2.31 V for 4 : 1 (Ti,Mn)O_x films (*i.e.*, E_F at 1.09 V_{RHE}). This E_F lowering occurred because the Mn 3d states created inside the TiO_2 bandgap hosted free carrier electrons.

Based on the valence XPS analyses, we assigned the potentials of band edges, Fermi levels, and IBs with respect to the RHE scale (right vertical axis), shown under flat-band conditions (Fig. 4b). At the liquid interface, the CB and VB edges of TiO_2 were located at −0.05 and 3.29 V_{RHE}, respectively.[40] For (Ti,Mn)O_x the Mn IB center was 1.17 ± 0.11 eV above the VB edge or at 2.31 ± 0.11 V_{RHE}. Under applied potentials, their relative positions were considered fixed.

Fig. 5a ("leaky TiO_2") was derived from a recent report (see ESI Discussions S3.1†), which was supported by direct *in situ* ambient-pressure XPS of the liquid junction interface of "leaky" TiO_2 and KOH(aq).[40] The band bending in the TiO_2 is due to the positive and immobile space charge of their oxygen vacancies. The charge density of Mn_2O_3 crystallites, due to the point defects in Mn_2O_3 bixbyite, was at the degenerately p-type doping level due to the Mn vacancy defects in this class of p-type oxides. The Mn IB was always partially filled with electrons that were transferred from nearby rutile TiO_2 crystallites. The high charge density of partially-filled Mn IB (>10^{21} cm^{-3}) was supported by the 47–50 Ω resistance of (Ti,Mn)O_x for a range of Mn composition (26–51 at% Mn). The stoichiometric TiO_2 achieved by ALD[23] and the lower formation energy of Mn_2O_3 than TiO_2 (ref. 41 and 42) ensured the metallic nature of the Mn IB states after annealing. The Mn_2O_3 nanocrystallites formed a conductive network throughout the (Ti,Mn)O_x coating.

Under bias, the band bending for TiO_2 and Mn_2O_3 follow their respective properties of charge density and band positions at the liquid interface. As shown in Fig. 5a, applying +1.8 V_{RHE} creates a band bending potential profile. This is because the ionic charge density of 10^{21} to 10^{23} cm^{-3} is typically observed at the TiO_2-liquid interfaces.[43] For the "leaky" TiO_2 with a Ti^{3+}-defect band, the positive space-charge density was calculated to be 2.1 × 10^{20} cm^{-3}, but its free-electron concentration was less than 10^{17} cm^{-3} due to electron trapping by the Ti^{3+}-defect band.[44] In contrast, the metallic Mn_2O_3 should accumulate holes under the applied potential. Accordingly, the Mn IB shifted its potential energy downward to align with the applied potential. As shown in Fig. 5b, at +1.8 V_{RHE}, the in-gap Mn states shifted to align with the E_F of Mn_2O_3 crystallites of (Ti,Mn)O_x due to their metallic behavior. Higher overpotentials would lead to increased band bending for the TiO_2 host oxide, but a shift in the position of the Mn intermediate band. This may enable other oxidation pathways, resulting in parasitic anodic current and an overall decrease in selectivity.

Under the applied potential of +1.8 V_{RHE} there exists a small and positive overpotential to the $2e^-$ water oxidation for H_2O_2 formation. Under such a small overpotential, the electron potential of the (Ti,Mn)O_x coatings lies more positive than the formal potential of the H_2O_2/H_2O couple, *i.e.*, 24 mV positive to $E(H_2O_2/H_2O)$. During operation, the energy levels of CB and VB of TiO_2 are fixed, or "pinned", at −0.05 and 3.29 V_{RHE}, respectively, and due to the semiconductor-like band bending of the TiO_2 bulk and the "unpinning" behavior of Mn-IB at the liquid-junction interface, the empty states of the Mn IB can precisely align with the energetics of H_2O_2 producing intermediates. Under a higher applied potential, *i.e.*, +2.3 V_{RHE}, there would exist a moderate overpotential for the $2e^-$ water oxidation, but such a potential also enables the other pathways including $1e^-$ water oxidation to produce radicals, leading to an overall

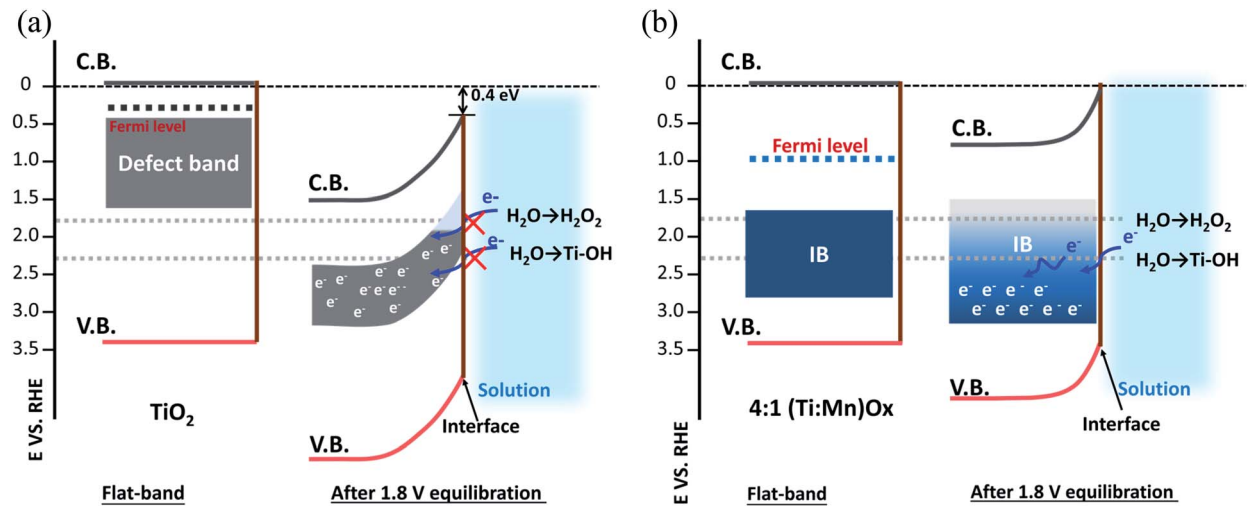

Fig. 5 Interfacial band energetics of semiconductive electrocatalysts. (a) "Leaky" TiO_2 and (b) 4 : 1 (Ti,Mn)O_x films. The left panel of each diagram was drawn under flat band conditions, and the right panel of each diagram was drawn where the electrode was poised at +1.8 V_{RHE} during water oxidation. Box height was drawn based on the estimated top edge of the Ti^{3+}-defect band or the Mn^{3+} intermediate band.

Published on 05 agosto 2021. Downloaded on 06/05/2026 15:02:15.

reduction in H_2O_2 production rates due to the reduced selectivity. Thus, the strategy for tuning the intermediate band towards highly selective electrocatalysis is best suited for the desired low-overpotential electrolysis and other strategies are therefore necessary for increasing geometric current density and, eventually, turnover frequency per site.

4. Conclusion

This study offered a theory-supported design of electrocatalytic surfaces that favor a H_2O_2 pathway. The authors design a surface that does not exhibit favorable kinetics for O_2 evolution, over-oxidize H_2O_2, nor disproportionate the as-produced H_2O_2. The mixed TiO_2/Mn_2O_3 nanocrystallites are chemically stable and protected by the TiO_2-rich surface. $(Ti,Mn)O_x$ coatings have been shown to be stable over 200 hours in modestly acidic and modestly basic solutions suggesting that those (Mn,Ti) sites are not as labile and soluble as the ordinary MnO_x sites. Their acid stability is comparable to the ordered ternary phases of recently reported Mn-based acid stable catalysts.[45]

This study elucidates a new strategy of introducing charge-transport IBs and led to the design of H_2O_2-producing surfaces that oxidize water to H_2O_2 with high selectivity at very low overpotentials. The Mn^{3+}-impurity IBs were created within the otherwise forbidden bandgap of TiO_2 which enhanced the electrical conductivity across the coating and matched the electronic states for H_2O_2-producing surface intermediates. Given the growing literature related to H_2O_2 selective catalysis, this approach is expandable to a range of host oxides that prevent H_2O_2 disproportionation to favor $2e^-$ H_2O_2 electrochemistry. However, this strategy is limited to the low overpotential regime, which limits the system to low current densities and requires further molecular or materials discovery for increasing turn-over frequency per active site.[11]

Author contributions

S. H. conceived the project. J. L., S. H., and Q. Z. designed the experiments. X. S. fitted and analyzed the valence XPS. J. L., G. C., and D. S., performed catalytic reactions and titration experiments. J. L., D. S., and Q. Z. performed XRD, XPS, and TEM characterizations and data analyses. J. L., S. H., X. S., Q. Z., and D. S. analyzed the data and co-wrote the manuscript. All co-authors discussed the results, finalized the conclusions, and edited the manuscript.

Conflicts of interest

Yale University has filed a provisional U.S. patent application directly related to the work described in this paper (patent application no. 62/843856, filed on 6 May 2019).

Acknowledgements

The authors would like to thank Dr Min Li at Yale's Materials Characterization Core (MCC) for his invaluable help with SEM, GIXRD, and XPS characterizations. The authors would like to acknowledge the start-up support from the Tomkat Foundation. J. L. would like to acknowledge the China Scholarship Council (CSC) for its financial support and the Donghua University Doctoral Innovation Fund Program (17D310606, 106-06-0019058).[3]

References

1 R. Ciriminna, L. Albanese, F. Meneguzzo and M. Pagliaro, *ChemSusChem*, 2016, **9**, 3374–3381.
2 J. M. Campos-Martin, G. Blanco-Brieva and J. L. G. Fierro, *Angew. Chem., Int. Ed.*, 2006, **45**, 6962–6984.
3 R. Hage and A. Lienke, *Angew. Chem., Int. Ed.*, 2006, **45**, 206–222.
4 M. Wehner, R. L. Truby, D. J. Fitzgerald, B. Mosadegh, G. M. Whitesides, J. A. Lewis and R. J. Wood, *Nature*, 2016, **536**, 451–455.
5 K. Kosaka, H. Yamada, K. Shishida, S. Echigo, R. A. Minear, H. Tsuno and S. Matsui, *Water Res.*, 2001, **35**, 3587–3594.
6 S. Fukuzumi, Y. Yamada and K. D. Karlin, *Electrochim. Acta*, 2012, **82**, 493–511.
7 G. Goor, J. Glenneberg, S. Jacobi, J. Dadabhoy and E. Candido, *Ullmann's Encycl. Ind. Chem.*, 2019, 1–40, DOI: 10.1002/14356007.a13_443.pub3.
8 D. W. Flaherty, *ACS Catal.*, 2018, **8**, 1520–1527.
9 S. Siahrostami, A. Verdaguer-Casadevall, M. Karamad, D. Deiana, P. Malacrida, B. Wickman, M. Escudero-Escribano, E. A. Paoli, R. Frydendal and T. W. Hansen, *Nat. Mater.*, 2013, **12**, 1137.
10 Z. W. Seh, J. Kibsgaard, C. F. Dickens, I. Chorkendorff, J. K. Nørskov and T. F. Jaramillo, *Science*, 2017, **355**, eaad4998.
11 J. Tang, T. Zhao, D. Solanki, X. Miao, W. Zhou and S. Hu, *Joule*, 2021, **5**, 1432–1461.
12 S. Mathew, F. Kuttassery, S. N. Remello, A. Thomas, D. Yamamoto, S. Onuki, Y. Nabetani, H. Tachibana and H. Inoue, *ChemPhotoChem*, 2018, **2**, 240–248.
13 Y. Ando and T. Tanaka, *Int. J. Hydrogen Energy*, 2004, **29**, 1349–1354.
14 X. Shi, S. Siahrostami, G.-L. Li, Y. Zhang, P. Chakthranont, F. Studt, T. F. Jaramillo, X. Zheng and J. K. Nørskov, *Nat. Commun.*, 2017, **8**, 701.
15 K. Zhang, J. Liu, L. Wang, B. Jin, X. Yang, S. Zhang and J. H. Park, *J. Am. Chem. Soc.*, 2020, **142**, 8641–8648.
16 J. C. Hill and K.-S. Choi, *J. Phys. Chem. C*, 2012, **116**, 7612–7620.
17 S. Y. Park, H. Abroshan, X. Shi, H. S. Jung, S. Siahrostami and X. Zheng, *ACS Energy Lett.*, 2019, **4**, 352–357.
18 Y. Jiang, P. Ni, C. Chen, Y. Lu, P. Yang, B. Kong, A. Fisher and X. Wang, *Adv. Energy Mater.*, 2018, 1801909.
19 C. Xia, S. Back, S. Ringe, K. Jiang, F. Chen, X. Sun, S. Siahrostami, K. Chan and H. Wang, *Nat. Catal.*, 2020, **3**, 125–134.
20 S. R. Kelly, X. Shi, S. Back, L. Vallez, S. Y. Park, S. Siahrostami, X. Zheng and J. K. Nørskov, *ACS Catal.*, 2019, **9**, 4593–4599.

 This journal is © The Royal Society of Chemistry 2021

Published on 05 agosto 2021. Downloaded on 06/05/2026 15:02:15.

21 A. Izgorodin, E. Izgorodina and D. R. MacFarlane, *Energy Environ. Sci.*, 2012, **5**, 9496–9501.
22 J. Zhang and Y. Nosaka, *J. Phys. Chem. C*, 2014, **118**, 10824–10832.
23 P. Nunez, M. H. Richter, B. D. Piercy, C. W. Roske, M. Cabán-Acevedo, M. D. Losego, S. J. Konezny, D. J. Fermin, S. Hu, B. S. Brunschwig and N. S. Lewis, *J. Phys. Chem. C*, 2019, **123**, 20116–20129.
24 T. Umebayashi, T. Yamaki, H. Itoh and K. Asai, *J. Phys. Chem. Solids*, 2002, **63**, 1909–1920.
25 V. E. Henrich and P. A. Cox, *The Surface Science of Metal Oxides*, Cambridge University Press, Cambridge, 1994.
26 R. J. Lad and V. E. Henrich, *Phys. Rev. B: Condens. Matter Mater. Phys.*, 1988, **38**, 10860–10869.
27 G. Siddiqi, Z. Luo, Y. Xie, Z. Pan, Q. Zhu, J. A. Röhr, J. J. Cha and S. Hu, *ACS Appl. Mater. Interfaces*, 2018, **10**, 18805–18815.
28 K. L. Pickrahn, A. Garg and S. F. Bent, *ACS Catal.*, 2015, **5**, 1609–1616.
29 R. Frydendal, E. A. Paoli, I. Chorkendorff, J. Rossmeisl and I. E. L. Stephens, *Adv. Energy Mater.*, 2015, **5**, 1500991.
30 A. Li, H. Ooka, N. Bonnet, T. Hayashi, Y. Sun, Q. Jiang, C. Li, H. Han and R. Nakamura, *Angew. Chem., Int. Ed.*, 2019, **58**, 5054–5058.
31 A. Plauck, E. E. Stangland, J. A. Dumesic and M. Mavrikakis, *Proc. Natl. Acad. Sci. U. S. A.*, 2016, **113**, E1973.
32 S. Hu, *Sustainable Energy Fuels*, 2019, **3**, 101–114.
33 X. Shi, Y. Zhang, S. Siahrostami and X. Zheng, *Adv. Energy Mater.*, 2018, 1801158.
34 E. Lobyntseva, T. Kallio, N. Alexeyeva, K. Tammeveski and K. Kontturi, *Electrochim. Acta*, 2007, **52**, 7262–7269.
35 Q. Zhu, M. Hinkle, D. J. Kim and J.-H. Kim, *ACS ES&T Engg*, 2021, **1**, 446–455.
36 K. Feng, H. Zhang, J. Gao, J. Xu, Y. Dong, Z. Kang and J. Zhong, *Appl. Phys. Lett.*, 2020, **116**, 191903.
37 L. Liu and A. Corma, *Nat. Catal.*, 2021, **4**, 453–456.
38 S. Siahrostami, G.-L. Li, V. Viswanathan and J. K. Nørskov, *J. Phys. Chem. Lett.*, 2017, **8**, 1157–1160.
39 V. Viswanathan, H. A. Hansen and J. K. Nørskov, *J. Phys. Chem. Lett.*, 2015, **6**, 4224–4228.
40 M. F. Lichterman, S. Hu, M. H. Richter, E. J. Crumlin, S. Axnanda, M. Favaro, W. Drisdell, Z. Hussain, T. Mayer, B. S. Brunschwig, N. S. Lewis, Z. Liu and H.-J. Lewerenz, *Energy Environ. Sci.*, 2015, **8**, 2409–2416.
41 N. Birkner and A. Navrotsky, *Proc. Natl. Acad. Sci. U. S. A.*, 2017, **114**, E1046.
42 M. R. Ranade, A. Navrotsky, H. Z. Zhang, J. F. Banfield, S. H. Elder, A. Zaban, P. H. Borse, S. K. Kulkarni, G. S. Doran and H. J. Whitfield, *Proc. Natl. Acad. Sci. U. S. A.*, 2002, **99**, 6476.
43 P. N. R. L. J. Lipkowski, *The Electrochemistry Of Novel Materials (Frontiers In Electrochemistry*, Wiley-VCH, 1993.
44 S. Hu, M. R. Shaner, J. A. Beardslee, M. Lichterman, B. S. Brunschwig and N. S. Lewis, *Science*, 2014, **344**, 1005.
45 L. Zhou, A. Shinde, J. H. Montoya, A. Singh, S. Gul, J. Yano, Y. Ye, E. J. Crumlin, M. H. Richter, J. K. Cooper, H. S. Stein, J. A. Haber, K. A. Persson and J. M. Gregoire, *ACS Catal.*, 2018, **8**, 10938–10948.